Computer Methods and Programs in Biomedicine 230 (2023) 107363

Contents lists available at ScienceDirect

Computer Methods and Programs in Biomedicine

journal homepage: www.elsevier.com/locate/cmpb

Gold nanorods assisted photothermal therapy of bladder cancer in mice: A computational study on the effects of gold nanorods distribution at the centre, periphery, and surface of bladder cancer

Jason KK Cheong[a,b], Ean H Ooi[a,b,*], Yeong S Chiew[b], Luca Menichetti[c], Paolo Armanetti[c], Mauro Comes Franchini[d], Elisa Alchera[e], Irene Locatelli[e], Tamara Canu[f], Mirko Maturi[d], Viktor Popov[a], Massimo Alfano[e]

[a] Ascend Technologies Ltd, Wessex House, Upper Market Street, Eastleigh, SO50 9FD, United Kingdom
[b] Mechanical Engineering Discipline, School of Engineering and Advanced Engineering Platform, Monash University Malaysia, Jalan Lagoon Selatan, 47500 Bandar Sunway, Selangor Malaysia
[c] CNR - Istituto di Fisiologia Clinica, Sede principale, Via G. Moruzzi 1, 56124 Pisa, Italy
[d] Department of Industrial Chemistry Toso Montanari, University of Bologna, Viale Risorgimento 4, 40136 Bologna, Italy
[e] Division of Experimental Oncology/Unit of Urology, URI, IRCCS Ospedale San Raffaele, Via Olgettina 60, 20132 Milan, Italy
[f] Experimental Imaging Center, Preclinical Imaging Facility, IRCCS San Raffele Scientific Institute, 20132 Milan, Italy

ARTICLE INFO

Article history:
Received 19 September 2022
Revised 12 January 2023
Accepted 19 January 2023

Keywords:
Bladder cancer
Photothermal therapy
Numerical simulation
GNR
Thermal ablation

ABSTRACT

Background and objectives: Gold nanorod-assisted photothermal therapy (GNR-PTT) is a cancer treatment whereby GNRs incorporated into the tumour act as photo-absorbers to elevate the thermal destruction effect. In the case of bladder, there are few possible routes to target the tumour with GNRs, namely *peri*/intra-tumoural injection and intravesical instillation of GNRs. These two approaches lead to different GNR distribution inside the tumour and can affect the treatment outcome.

Methodology: The present study investigates the effects of heterogeneous GNR distribution in a typical setup of GNR-PTT. Three cases were considered. Case 1 considered the GNRs at the tumour centre, while Case 2 represents a hypothetical scenario where GNRs are distributed at the tumour periphery; these two cases represent intratumoural accumulation with different degree of GNR spread inside the tumour. Case 3 is achieved when GNRs target the exposed tumoural surface that is invading the bladder wall, when they are delivered by intravesical instillation.

Results: Results indicate that for a laser power of 0.6 W and GNR volume fraction of 0.01%, Case 2 and 3 were successful in achieving complete tumour eradication after 330 and 470 s of laser irradiation, respectively. Case 1 failed to form complete tumour damage when the GNRs are concentrated at the tumour centre but managed to produce complete tumour damage if the spread of GNRs is wider. Results from Case 2 also demonstrated a different heating profile from Case 1, suggesting that thermal ablation during GNR-PTT is dependant on the GNRs distribution inside the tumour. Case 3 shows similar results to Case 2 whereby gradual but uniform heating is observed. Cases 2 and 3 show that uniformly heating the tumour can reduce damage to the surrounding tissues.

Conclusions: Different GNR distribution associated with the different methods of introducing GNRs to the bladder during GNR-PTT affect the treatment outcome of bladder cancer in mice. Insufficient spreading during intratumoural injection of GNRs can render the treatment ineffective, while administered via intravesical instillation. GNR distribution achieved through intravesical instillation present some advantages over intratumoural injection and is worthy of further exploration.

* Corresponding author.
E-mail addresses: ooi.ean.hin@monash.edu, eanhin@ascendtechnologies.co.uk (E.H. Ooi).

https://doi.org/10.1016/j.cmpb.2023.107363

1. Introduction

Current methods of bladder cancer treatment rely on the stage of cancer growth. When detected early, transutheral resection of bladder tumour (TURBT) is often the method of choice. However, if the cancer is detected late, or when the tumour has become muscle invasive, radial cystectomy is often the only choice of treatment. Both methods are not ideal as they are associated with various complications. These bladder cancer treatment methods are far from ideal, which calls for the development of more reliable treatments with minimal risks to be made readily available to the public.

Nanoparticle-assisted photothermal therapy (NPTT) has demonstrated great potential as a cancer treatment technique [1]. The nanoparticles act as photo-enhancers that efficiently absorb and convert light into heat, thus inducing cell necrosis in the tissue where they bind to via hyperthermia and thermal coagulation [2–6]. Among the different types of nanoparticles that have been investigated for use in NPTT, gold nanorods (GNRs) by far have received the greatest interest amongst researchers and have been extensively studied for this purpose [7–10]. The key factor possessed by GNRs is the ability for their absorption to be tuned to peak at designated wavelengths by adjusting the aspect ratio of the GNR. This factor enables GNRs to be used with lasers employing higher wavelengths, usually in the near infrared region, as this allows for deeper penetration into the human tissue. The application of GNRs in gold nanorod-assisted photothermal therapy (GNR-PTT) is further supported by the good bioconjugation abilities of GNRs [11–13], which allows various cancer-targeting antibodies to be conjugated for the selective destruction of tumours.

The application of GNRs extends beyond photothermal therapy. For example, Nair et al. [14–16] developed a multimodal imaging and therapeutic system, by incorporating fluorescent chemotherapeutic drugs into the GNRs to facilitate fluorescence imaging and targeted chemotherapy through the release of drugs by the GNRs within the targeted tissue. Narayanan et al. [17] achieved combined photothermal and photodynamic therapies of breast cancer by customising a nanotheranostic probe involving GNRs and macrocyclic host cucurbituril sandwiched between two GNRs. More recently, Alchera et al. [18] demonstrated the potential for early bladder cancer diagnosis by using photoacoustic imaging of tumour targeted GNRs.

Several preclinical studies investigated the feasibility of the treatment of GNR-PTT against solid tumours by delivering the nanoparticle by intravenous (IV) injection or via intratumoural injection. However, for bladder cancer treatment, the structure of the bladder offers the possibility to deliver the nanoparticles through catheters via intravesical instillation, an option that has recently been explored by using targeted GNRs [19]. The selection of IV or intravesical delivery of GNRs into bladder cancer for GNR-PTT raises the question of how GNRs are distributed inside the tumour under different delivery mode and its potential impact on the treatment outcome. For instance, the accumulation in the tumour of GNRs delivered by IV injection is likely to cause the GNR to accumulate around the neovessels or to spread far from the entry site. Furthermore, heterogeneity in the tumour stromal and microenvironment may lead to heterogeneous GNR distribution inside the tumour [20]. Conversely, GNRs that are introduced via intravesical instillation are likely confined to the tumour surface that is in contact with the GNR solution. Consequently, the effective presence of the GNR is not only lower, but heat absorption inside the tumour also becomes restricted to the bladder surface. These heterogeneous and surface GNR distributions are different from the homogeneous distribution assumed by the existing computational studies on GNR-PTT of bladder cancer reported in the literature [21–23], thus raising the need of more accurate modelling.

The aim of the present study is to understand the effects of a heterogeneous GNR distribution inside the tumour on the outcome of GNR-PTT during bladder cancer treatment. Additionally, the impact of a surface GNR distribution, a scenario that arises from the attachment of GNRs during intravesical instillation is also investigated. A computational model was developed, where simulations were carried out numerically using a coupled Monte Carlo-finite element model framework similar to that presented by Cheong et al. [24]. It is expected that the results obtained from the present study will shed light on the role of GNR distribution on GNR-PTT and provide useful information that allows the development of more reliable protocols of GNR-PTT for bladder cancer treatment.

2. Methodology

2.1. Model geometry

The model of the mouse bladder was constructed based on the images obtained from an MRI scan of a female C57/BL6 mouse at 8 week of age (IACUC #942). Points were manually annotated along the bladder boundary for each of the 10 slices containing the bladder. Next, the coordinates of the annotated points were imported into SolidWorks, where the *loft* function was used to connect the points and reconstruct the 3D geometry. A cuboid measuring 20 mm in length, 16 mm in width and 11 mm in height was built around the bladder such that the boundary representing the skin surface is 0.3 mm from the top surface of the bladder, matching the thickness observed in the MRI slices. This is illustrated in Fig. 1a, where the orientation considered assumed the mouse to be lying on its back. A tumour was generated along the topside of the bladder wall, resembling an irregular cylinder with a radius of 0.5 mm and an estimated volume of 0.192 mm^3.

To investigate the heterogeneous distribution of GNRs, the geometry of the tumour was modified to represent three different cases. In the first case (Case 1), the GNRs were assumed to be distributed only at the interior region of the tumour covering a radius of r_i from the central axis of the tumour. This is indicated by the red zone in Fig. 1b. The outer region of the tumour was assumed to be free of GNRs. In the second case (Case 2), GNRs were assumed to occupy the outer region of the tumour, covering a thickness defined by r_o. This is illustrated in Fig. 1c. In the present study, the effects of different values of r_i and r_o, which describe the different degree of GNR spread inside the tumour, were examined. As Case 2 is essentially the reverse of Case 1, a new parameter r_{rat} was introduced to consistently quantify the different GNR spread inside the tumour:

$$r_{rat} = \frac{l_{GNR}}{r_{tum}}, \tag{1}$$

where r_{tum} is the radius of the tumour, in the current case 0.5 mm, and l_{GNR} is the value that defines the spread of the GNR, such that $l_{GNR} = r_i$ in Case 1 and $l_{GNR} = r_o$ in Case 2. Note that $r_{tum} = r_i + r_o$ in all cases.

The third case (Case 3) represents the condition that arises from the attachment of GNRs onto the tumour surface following intravesical instillation. This was achieved in the model by adding a thin region at the bottom of the tumour as shown in Fig. 1d. The thickness of this region was set to 0.025 mm, which is approximately one-eighth of tumour's height. This was deemed to be sufficiently small for the GNR distribution to mimic the surface attachment following intravesical instillation.

Laser irradiation was carried out using a laser beam with a radius of 1.5 mm and with a wavelength that is identical to the wavelength of the GNRs tuned to reach of the peak absorbence, i.e., 778 nm (see Section 2.7.2). The laser was placed just above the skin surface in-line with the centre of the tumour. The direction of

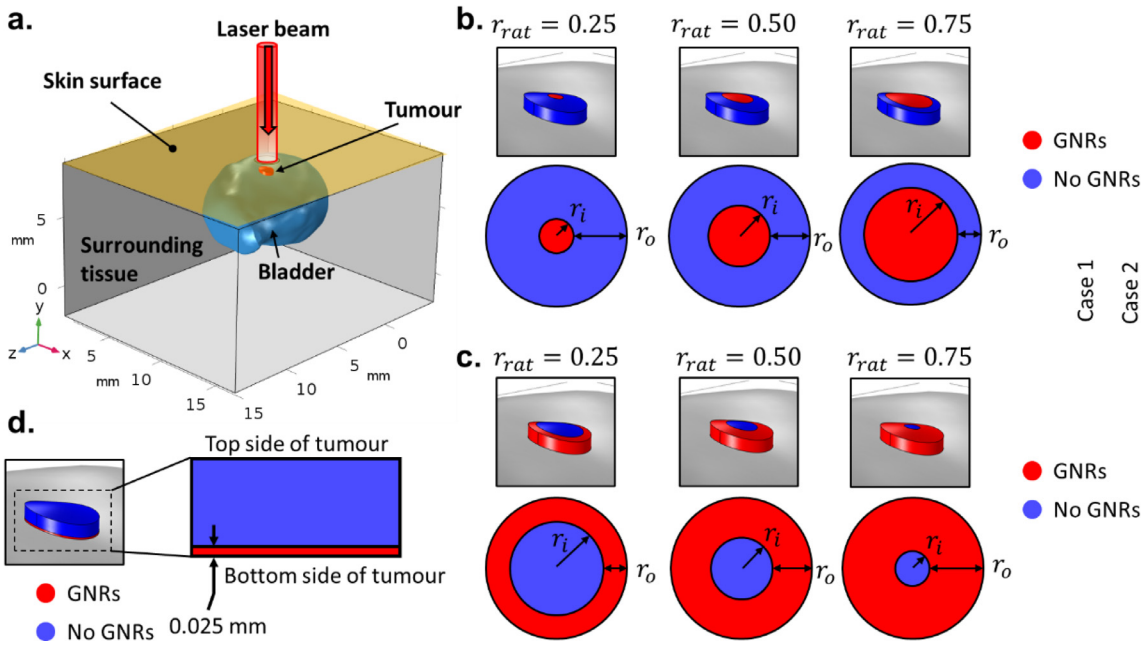

Fig. 1. a) Model setup developed in the present study indicating the whole mouse bladder and the surrounding tissue; b) distribution of GNRs inside the tumour in Case 1; c) distribution of GNRs inside the tumour in Case 2 and d) distribution of GNRs along the bottom surface of the tumour in Case 3. The red arrow in (a) indicate the direction of the laser beam, which is downwards and perpendicular to the skin surface.

the laser beam was assumed to be directed vertically downwards, such as shown in Fig. 1a.

2.2. Monte Carlo simulations

The propagation of laser inside the surrounding tissue, bladder, tumour and the urine were simulated using the Monte Carlo method, which is widely regarded as the gold standard for modelling light propagation [25–27]. Details of the Monte Carlo algorithm are already published in several textbooks and online sources; hence, they will not be presented here. In the present study, the Monte Carlo method was implemented using the open-source code ValoMC [27]. The code was written in MATLAB and performs a mesh-based Monte Carlo algorithm that simulates the propagation of light in geometries that are defined by a series of unstructured mesh, such as triangles (in 2D) and tetrahedrons (in 3D). The application of tetrahedrons is especially useful when discretising complex shapes and geometries such as the bladder. The algorithm requires four inputs, i.e., the absorption coefficient (μ_a), the scattering coefficient (μ_s), the scattering anisotropic factor (g) and the refractive index (n). Upon solving, the algorithm outputs the fluence distribution, which was exported into COMSOL Multiphysics for heat transfer simulations to be carried out.

2.3. Heat transfer model

Heat transfer inside the surrounding tissue, bladder and tumour can be expressed using the Pennes bioheat equation [28, 29]:

$$\rho_t c_t \frac{\partial T_t}{\partial t} = \nabla \cdot (k_t(T_t)\nabla T_t) + \rho_b c_b \omega_b(\Omega)(T_b - T_t) + \mu_{a,t}\Phi_t P_{laser} \tag{2}$$

where T_t is tissue temperature, ρ_t, c_t and $k_t(T)$ represent the density, specific heat and temperature-dependant thermal conductivity, respectively, ρ_b and c_b are the density and specific heat of blood, respectively, $\omega_b(\Omega)$ is the damage-dependant blood perfusion rate, with Ω the thermal damage parameter, T_b is the arterial blood temperature, $\mu_{a,t}$ is the absorption coefficient, Φ_t is the fluence distribution obtained from the Monte Carlo simulations and P_{laser} is the laser power. Prior investigations have found that the metabolic heat generation provides negligible contribution when compared to the heat generated during photothermal ablation. As such, this term was purposefully omitted from Eq. (2).

Heat transfer inside the urine domain is described using the conduction-convection equation:

$$\rho_f c_f \frac{\partial T_f}{\partial t} + \mathbf{u} \cdot \nabla T_f = \nabla \cdot \left(k_f\left(T_f\right)\nabla T_f\right) + \mu_{a,t}\Phi_t P_{laser}, \tag{3}$$

where the subscript 'f' represents urine inside the bladder and $\mathbf{u} = (u,\ v,\ w)$ is the vector field describing the velocity of urine flow inside the bladder in the x-, y- and z-directions. The velocity field can be obtained by solving in the urine domain the Navier-Stokes equations:

$$\rho_f \frac{\partial \mathbf{u}}{\partial t} + \rho_f(\mathbf{u} \cdot \nabla \mathbf{u}) = -\nabla p + \mu_f \nabla^2 \mathbf{u} + \rho_f\left(T_f\right)\mathbf{g}, \tag{4}$$

$$\rho_f \nabla \cdot \mathbf{u} = 0, \tag{5}$$

where p is pressure, μ_f is the dynamic viscosity of urine and $\mathbf{g}$ is the gravitational acceleration that acts in the negative y-direction with respect to the bladder orientation shown in Fig. 1a. The last term on the right-hand side of Eq. (4) represents the thermally induced buoyant forces acting on the urine inside the bladder and can be described using the Boussinesq approximation:

$$\rho_f\left(T_f\right) = \rho_{ref}\left[1 - \beta_f\left(T_f - T_{ref}\right)\right], \tag{6}$$

where ρ_{ref} is the urine density evaluated at reference temperature $T_{ref} = T_{body} = 37°C$ and β_f is the urine thermal expansion coefficient. The urine was assumed to be a Newtonian fluid, while flow of urine inside the bladder was assumed to be laminar with negligible viscous dissipation.

2.4. Cell death model

Part of the aim of this study is to achieve thermal ablation that can be described as cell necrosis or thermal coagulation. To cal-

culate the formation of thermal coagulation, the differential equation describing the Arrhenius rate of thermal coagulation was used [30]:

$$\frac{d\Omega(x,y,z,t)}{dt} = Ae^{-\frac{\Delta E}{R_c T(x,y,z,t)}}, \tag{7}$$

where Ω is a parameter that quantifies the amount of thermal coagulation, A is the frequency factor, ΔE is the activation energy required to cause irreversible thermal damage and R_c is the universal gas constant. The values of Ω calculated from Eq. (6) represent the percentage probability of cell destruction at a specific area caused by temperature rise. A value of $\Omega = 1$ is commonly used to represent a 63% probability of cell death [31]. However, the present study implemented a stricter criterion, where a threshold of $\Omega = 4.6$, which represents a 99% probability of cell death, was used to quantify thermal damage [32].

Using the definition of thermal damage, it is also possible to quantify the percentage by volume of a particular domain that has successfully undergo thermal coagulation. This is given by:

$$PD = 100\% \times \frac{V_{\Omega>4.6}}{V_{region}}, \tag{8}$$

where $V_{\Omega > 4.6}$ represents the volume of region pertaining to Ω values greater than 4.6 and V_{region} is the total volume of the specified region. A value of PD of 100% implies that the entire domain has been completely ablated. It is the aim of GNR-PTT in bladder cancer treatment to achieve $PD = 100\%$ inside the tumour while minimising the value across the bladder and the surrounding tissue.

2.5. Initial condition

Light propagation was assumed to occur at a much shorter timescale than heat transfer; hence, the Monte Carlo simulations can be decoupled from the heat transfer simulations. The initial temperature of the model was obtained by solving Eqs (2) to (6) at steady state without any exposure to laser, i.e., by prescribing the time derivative in the left-hand side of Eqs (2), (3) and (4) to be zero and by letting $P_{laser} = 0$.

2.6. Boundary conditions

The skin surface was assumed to be exposed to ambient conditions, where heat transfer via convection takes place. A Robin condition was thus prescribed here:

$$-k_t(T_t)\frac{\partial T_t}{\partial n} = h_{amb}(T_t - T_{amb}), \tag{9}$$

where h_{amb} is the convective heat transfer coefficient between the skin and the ambient, and T_{amb} is the ambient temperature. The bottom surface of the surrounding tissue was assumed to be sufficiently far from the laser focal zone, such that normothermoregulation can successfully maintain the temperature here at basal level. Therefore, the boundary condition across this surface is given by:

$$T_t = T_{body} = 37^{\circ}\mathrm{C}, \tag{10}$$

For the hydrodynamics model, stationary no-slip condition was prescribed across the inner surfaces of the bladder wall, such that:

$$\mathbf{u} = 0. \tag{11}$$

2.7. Material properties

2.7.1. Thermal properties

The thermal properties used in the present study are listed in Table 1. Except for the tumour, the values presented in Table 1 were obtained from the IT'IS database [33]. Due to the lack of information regarding bladder cancer thermal properties, those of liver cancer were used instead. This is justified as the thermal properties of non-cancerous liver and bladder differ by less than 1.5% [38]. Because of the low GNR volume fractions (v/v) considered in the present study (see Section 3), the presence of the GNR was assumed to have negligible influence on the thermal properties of the tumour. These volume fractions are in line with the ranges used in previous literature studies [8, 22, 38]. All parameters were assumed to be homogeneous, isotropic, and independent of the physical variables considered in the present study, except for the thermal conductivity, which was assumed to increase linearly with temperature at a rate of 1.5% for every 1 °C increase in temperature [41]. This assumption was applied to all the domains including the urine inside the bladder.

Table 1
Thermal properties employed in the present study.

Parameter	Value	Source
Bladder		
Thermal conductivity, k (W/m²K)	0.52	[33]
Density, ρ (kg/m³)	1086	[33]
Specific heat, c (J/kg·K)	3581	[33]
Blood perfusion rate, ω_b (1/s)	0.0014	[33]
Frequency factor, A (1/s)	3.3×10^{38}	[34]
Activation energy, ΔE (J/mol)	2.57×10^{5}	[34]
Tumour		
Thermal conductivity, k (W/m²K)	0.49	[35]
Density, ρ(kg/m³)	1090	[35]
Specific heat, c (J/kg·K)	3421	[35]
Blood perfusion rate, ω_b(1/s)	0.00165	[35]
Frequency factor, A (1/s)	1.46×10^{52}	[36]
Activation energy, ΔE (J/mol)	3.43×10^{5}	[36]
Surrounding tissue		
Thermal conductivity, k (W/m²K)	0.21	[33]
Density, ρ(kg/m³)	911	[33]
Specific heat, c (J/kg·K)	2348	[33]
Blood perfusion rate, ω_b(1/s)	0.0005	[33]
Frequency factor, A (1/s)	1.61×10^{45}	[37]
Activation energy, ΔE (J/mol)	3.06×10^{5}	[38]
Urine		
Thermal conductivity, k (W/m²K)	0.56	[33]
Density, ρ (kg/m³)	1024	[33]
Specific heat, c (J/kg·K)	4178	[33]
Thermal expansion coefficient, β_f (1/K)	3.374×10^{-4}	[39]
Dynamic viscosity, μ_f (Pa.s)	0.0007	[39]
Constants		
Universal gas constant, R_c (J/mol·K)	8.314	
Ambient temperature, T_{amb} (°C)	25	
Ambient convection coefficient, h_{amb} (W/m²K)	3	

Studies on porcine have shown that blood perfusion in kidneys increases nonlinearly with temperature [34]. Below 45 °C, biological tissue responds to the increase in temperature by increasing the blood flow through vasodilation [42]. Further increase in temperature results in vascular stasis, which eventually leads to a decrease in blood perfusion. Blood perfusion stops when complete cell necrosis has occurred. This temperature-dependant behaviour of blood perfusion can be expressed as a piecewise homogeneous function of Ω given by [34, 43]:

$$\omega_b(\Omega) = \omega_{b,ref} \times \begin{cases} 0.3\left(1-e^{-\Omega}\right)+0.01, & \Omega \le 0.02 \\ -0.13\left(1-e^{-\Omega}\right)+0.0186, & 0.02 < \Omega \le 0.08 \\ -0.0079\left(1-e^{-\Omega}\right)+0.00884, & 0.08 < \Omega \le 3.5 \\ -0.0387\left(1-e^{-\Omega}\right)+0.0387, & 3.5 < \Omega \le 4.6 \end{cases}, \tag{12}$$

where $\omega_{b,ref}$ represents the blood perfusion rate at body temperature.

Eq (12) was applied only to the bladder and surrounding tissues, but not to the tumour. This is because of the limited ability

Table 2
Optical parameters and the peak absorption and scattering coefficients at volume fraction, $\phi = 0.001$, 0.005 and 0.01%.

Parameter	Value	Source
Free electron density, n_o (1/m^3)	5.9×10^{28}	*
Permittivity of vacuum, ε_o (F/m)	8.85×10^{-12}	*
Electron charge, e (C)	1.6×10^{-19}	*
Mass of electron, m_e (kg)	9.1×10^{-31}	*
Fermi velocity, v_F (m/s)	1.39×10^{6}	*
Mean free path of electron (m)	42×10^{-9}	[48]
Absorption coefficient, μ_a (1/mm)		
Bladder	0.02	[45]
Surrounding tissue	0.105	[49]
Urine	0.002	[46]
Tumour embedded with GNR		
$\phi = 0.001\%$	4.29	¥
$\phi = 0.005\%$	21.47	¥
$\phi = 0.01\%$	42.93	¥
Scattering coefficient, μ_s (1/mm)		
Bladder	4.41	[45]
Surrounding tissue	11.16	[49]
Urine	1	[46]
Tumour embedded with GNR		
$\phi = 0.001\%$	0.052	¥
$\phi = 0.005\%$	0.261	¥
$\phi = 0.01\%$	0.521	¥

*Constants; ¥ Estimated using Mie-Gans theory.

of tumours to increase its blood flow in response to heat [42]. For the tumour, a more conservative form of damage-dependant blood perfusion was adopted:

$$\omega_b(\Omega) = \omega_{b,ref} \times \begin{cases} 1, & \Omega < 4.6 \\ 0, & \Omega \geq 4.6 \end{cases}, \tag{13}$$

Eq (13) implies that blood perfusion is only present in domains that have not been completely ablated.

2.7.2. Optical properties

The optical properties used in this study are presented in Table 2. The refractive indices and scattering anisotropic factors of all domains were chosen to be 1.4 and 0.9, respectively [44]. It should be noted that optical properties for mice bladder are not available in literature. Hence, the values used are that of a generalised bladder model developed from porcine [40]. For the urine, the absorption coefficient, scattering coefficient and refractive index were assumed to be that of water. The scattering anisotropic factor for the urine was chosen to be 1, implying that photon propagation inside the urine domain is purely forward scattering [46].

Unlike thermal properties, the influence of the GNR inside the tumour on the optical properties of the domain cannot be ignored. These values were obtained from the Mie-Gans theory [47] and they vary depending on the volume fraction of GNR inside the tumour. In the present study, the size of all the GNRs was assumed to be uniform, with a width of 10 nm and an aspect ratio of 3.8, giving peak absorbence at a wavelength of 778 nm. For more details on the calculation of the tumour-GNR optical properties, readers may refer to Appendix A.

2.8. Mesh convergence and model validation

Mesh convergence and model validation play vital roles in any computational simulation. The aim of performing a mesh convergence study is to obtain solutions that are not affected by the mesh density, while minimising the computational resources required to achieve the solution. On the other hand, model validation compares the attained solution to experimental studies to ensure the accuracy of the physics applied and can achieve results that are in line with real-life experiments. The model in this study has already passed both the mesh convergence and model validation studies, with the specifics documented in our previous work [24].

3. Results

As mentioned in Section 1, this study seeks to investigate the effects of heterogeneous distribution of GNRs during GNR-PTT of bladder cancer in mice. To facilitate this investigation, a preliminary study was conducted to determine the appropriate values for the combination of laser power (P_{laser}) and GNR volume fraction (ϕ) to achieve an effective treatment outcome. For this purpose, laser power of 0.4 and 0.5 W, and GNR volume fraction of 0.001, 0.005 and 0.01% were investigated. The GNRs were assumed to be homogeneously distributed across the entire tumour bulk volume, i.e., $r_{rat} = 1$. This allows for the results to double as a control for comparison with the present study. The results from the preliminary study, which are presented in Appendix B, suggest that a power rating of at least 0.5 W and a GNR volume fraction of $\phi = 0.01\%$ is required to achieve complete tumour ablation.

In Cases 1 to 3, GNRs were assumed to be present in selected regions of the tumour, while in the control case, GNRs are present homogeneously in the tumour volume. As such, the effective presence of GNRs is lower in each case when compared to the control. With that in consideration, the GNR volume fraction was set to 0.01%, while two laser powers were considered, namely 0.5 and 0.6 W.

The results obtained for Cases 1, 2 and 3 are presented separately next.

3.1. Case 1 ($l_{GNR} = r_i$)

Three values of r_{rat} were considered, namely 0.25, 0.5 and 0.75, with the GNR distribution in the tumour shown in Fig. 1b. Fig. 2a presents the contours of the temperature distribution obtained at $t = 30$ s for the three values of r_{rat} considered. Results from the control case ($r_{rat} = 1$), where GNRs are homogeneously distributed throughout the entire tumour, are also shown for comparison purposes. The maximum temperature, which was achieved within 30 s of laser irradiation, increases with r_{rat}. These temperatures were recorded at the skin surface and ranged from 50.7 ($r_{rat} = 0.25$) to 56.0 °C ($r_{rat} = 1$). The yellow arrows in Fig. 2a indicate that the region of elevated temperature in the tumour corresponds to the location where GNR was assumed to be located. This region expands as r_{rat} increases.

These results are within expectations as the shape of the temperature distribution demonstrates that heat is generated at two different locations during GNR-PTT. The first location is at the skin surface, where the maximum temperature was recorded corresponding to the point of the incident laser. The second location is at the region of elevated temperature within the tumour, where the laser interacts with the GNRs to generate heat. For a fixed volume fraction of GNR introduced into the tumour, an increase in r_{rat} increases the quantity of GNRs available for the absorption of photons and their conversion into heat, thus resulting in a more intense heating. Fig. 2b presents the contours of temperature distribution for each value of r_{rat} after 600 s of laser irradiation. The increase in maximum temperature from 63.9 ($r_{rat} = 0.25$) to 70.8 °C ($r_{rat} = 1$) corresponded to the increase in values of r_i. The heating trend remains unchanged with respect to time.

Fig. 3a shows the contours of Ω after 600 s of laser irradiation. The colour scale was capped at 4.6, where regions of dark red indicate complete thermal damage ($\Omega > 4.6$, see Section 2.4). For the case where $r_{rat} = 0.25$, the increase in Ω is observed to begin at the top of the tumour as the heat generation occurs in the region where the GNRs are located. While no thermal damage was found for $r_{rat} = 0.25$, as indicated by the value of Ω smaller than 4.6,

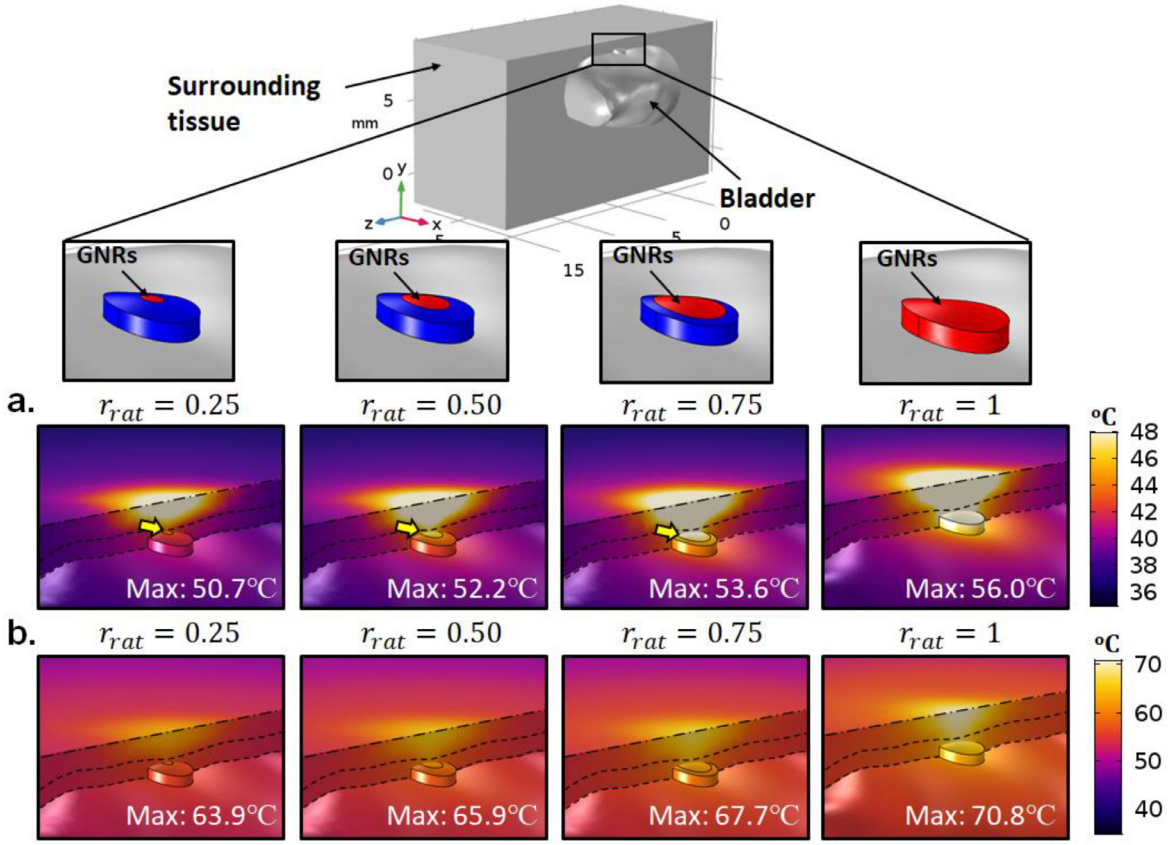

Fig. 2. Contours of the temperature distribution for all values of r_{rat} in Case 1 across the tumour, bladder and across the surrounding tissue at a) $t = 30$ s and b) $t = 600$ s after laser irradiation of 0.5 W. The temperature scale of a) was capped at 48 °C for better visualisation. Colour scale shows the temperature in °C. Top and bottom dashed lines indicate the outer and inner walls of the bladder, respectively. Dashed-dotted lines indicate the top surface of the surrounding tissue, i.e., the skin surface.

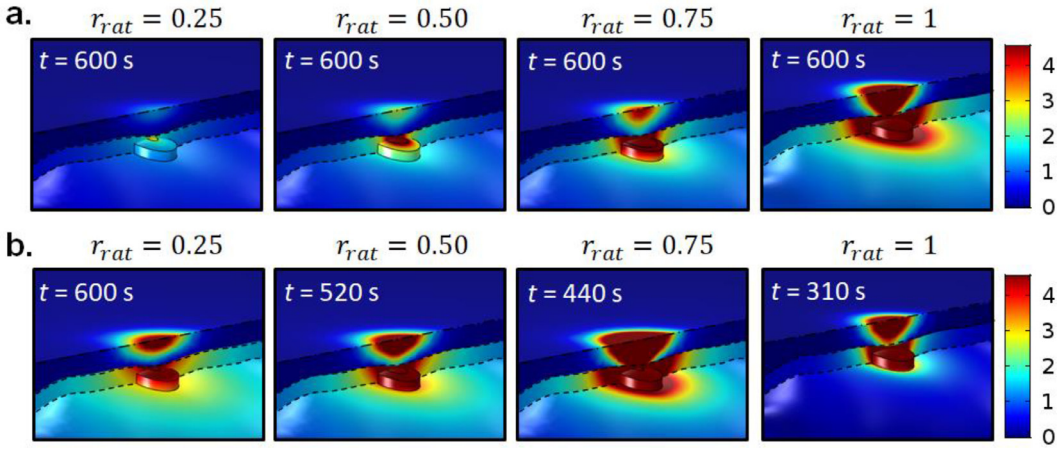

Fig. 3. Contours of the thermal damage parameter Ω for all values of r_{rat} in Case 1 across the tumour, bladder, and across the surrounding tissue at a) $t = 600$ s and $P_{laser} = 0.5$ W and b) $P_{laser} = 0.6$ W at time when complete tumour ablation was achieved. Colour scale shows the values of Ω capped at 4.6 such that regions in dark red represent regions that are thermally damaged. Top and bottom dashed lines indicate the outer and inner walls of the bladder, respectively. Dashed-dotted lines indicate the top surface of the surrounding tissue, i.e., the skin surface.

the other values of r_{rat} (0.5 and 0.75) recorded significant thermal damage, with 95% of the tumour sustaining thermal damage for the case of $r_{rat} = 0.75$. Nevertheless, this was still lower than the control where complete tumour damage was found ($PD = 100\%$). Of note, $r_{rat} = 0.25$ indicated a lower GNR presence due to the smaller volume, which resulted in insufficient heating within the tumour and consequently an absence of tumour damage.

Table 3 summarises the values of PD calculated across the tumour domain for each value of r_{rat}. As defined in Eq (8), a value of $PD = 100\%$ implies that the entire tumour region has value of $\Omega > 4.6$, i.e., has achieved completed tumour ablation. To further understand how the formation of thermal damage is linked to the temperature attained inside the tumour, the minimum and maximum temperatures $[T_{min}, T_{max}]$ reached inside the tumour after 600 s are also presented in Table 3. At a laser power of 0.5 W, none of the models under Case 1 attained complete tumour ablation, which may be explained by the failure to heat the entire tumour to temperatures beyond 60 °C, the threshold required for

Table 3
Values of *PD* (%) calculated for the tumour domain and $[T_{min},T_{max}]$ inside the tumour obtained in Cases 1, 2 and 3 after 600 s of laser irradiation.

	PD (%)					
	P_{laser} = 0.5 W			P_{laser} = 0.6 W		
	r_{rat} = 0.25	r_{rat} = 0.50	r_{rat} = 0.75	r_{rat} = 0.25	r_{rat} = 0.50	r_{rat} = 0.75
Case 1	0	23.6%	94.7%	73.6%	100%	100%
Case 2	92.3%	100%	100%	100%	100%	100%
Case 3	14.2%			100%		
	$[T_{min},T_{max}]$ (°C)					
	P_{laser} = 0.5 W			P_{laser} = 0.6 W		
	r_{rat} = 0.25	r_{rat} = 0.50	r_{rat} = 0.75	r_{rat} = 0.25	r_{rat} = 0.50	r_{rat} = 0.75
Case 1	[55.6, 58.6]	[57.2, 62.0]	[58.8, 64.3]	[59.2, 62.7]	[61.2, 66.9]	[63.1, 69.6]
Case 2	[58.9, 61.4]	[61.0, 65.2]	[61.3, 66.6]	[63.2, 66.2]	[65.6, 70.6]	[66.1, 72.4]
Case 3	[58.1, 59.9]			[62.2, 64.3]		

thermal coagulation to occur immediately [50]. This can be linked to the temperature reached inside the tumour after 600 s of laser irradiation.

To account for the low presence of GNRs due to the heterogeneous GNR distribution, simulations using a higher laser power of 0.6 W were carried out and the resulting thermal damage contours, *PD* values and temperature range $[T_{min},T_{max}]$ are presented in Fig. 3b and Table 3, respectively. By increasing the laser power to 0.6 W, all values of r_{rat}, except for r_{rat} = 0.25, successfully achieved complete tumour ablation (*PD* = 100%). In the cases in which *PD* = 100% was achieved, the range of temperature reached inside the tumour exceeded the 60 °C thermal coagulation threshold, further supporting the argument for cell death. The case of r_{rat} = 0.25 recorded 73% destruction across the tumour. Although complete tumour ablation was achieved for the remaining values of r_{rat}, the required time differed in each case. The time required for the cases of r_{rat} = 0.5 and 0.75 were 520 and 440 s, respectively, while the control case required only 310 s.

It is important to point out that achieving *PD* = 100% inside the tumour does not necessarily reflect an optimum treatment outcome. The results in Fig. 3b show the degree of thermal damage in the bladder and the surrounding tissue. Although the formation of thermal damage is small, r_{rat} = 0.5 recorded the least amount of damage to the bladder and the largest amount of damage to the surrounding tissue, close to the skin surface where the laser beam is introduced. Conversely, the control recorded the largest amount of damage to the bladder and the least amount of damage to the surrounding tissue adjacent to the skin. This may be attributed to the larger amount of GNRs and the shortest irradiation time for ablation.

Damage to the bladder is primarily caused by heat conduction from the GNRs within the tumour mass. Therefore, a larger presence of GNRs (represented by large values of r_{rat}) would induce greater heat generation and consequently increase the heat conduction to the bladder. A similar inference can be made for the damage to the surrounding tissue, specifically on the skin surface. These findings suggest that the different values of r_{rat}, which mimicked the different spread of GNRs from the tumour centre following intratumoural injection can affect the treatment requirements in terms of treatment duration and the amount of damage sustained by the tumour, the bladder, and the surrounding tissue.

3.2. Case 2 ($l_{GNR} = r_o$)

Similar to Case 1, three values of r_{rat} were considered for Case 2, namely 0.25, 0.5 and 0.75. The distribution of GNRs within the tumour for each value of r_{rat} is presented in Fig. 1c. Fig. 4a illustrates the temperature distributions obtained for Case 2. As expected, the location of maximum temperature was found at the skin surface that is exposed to laser irradiation. Fig. 4b presents the contours of thermal damage after 600 s of laser irradiation. The corresponding values of *PD* and $[T_{min},T_{max}]$ are presented in Table 3. For laser power of 0.5 W, and r_{rat} = 0.5 and 0.75, complete tumour ablation was achieved, unlike in Case 1 (see Section 3.1 and Table 3). The main reason for this is the surface area of GNR that is exposed to the laser. The surface area of the outer ring is larger than the inner circle for the same r_{rat} (see Fig. 1a). For comparison, the largest surface area in Case 1 was 0.455 mm^2 for the case of r_{rat} = 0.75, while the surface area for r_{rat} = 0.75 in Case 2 was 0.764 mm^2. A larger surface area allows greater exposure of the GNRs to the laser, which increases the heat generation inside the tumour to levels that are sufficiently high to induce complete tumour ablation.

Since r_{rat} = 0.25 did not achieve complete tumour ablation (see the black arrow in Fig. 4b), simulations using 0.6 W were conducted. The thermal damage obtained is presented in Fig. 5. It was found that the time taken to reach complete tumour ablation for r_{rat} = 0.25, 0.5 and 0.75 were 430, 350, and 330 s respectively. Comparison of the results between Cases 1 and 2 for a laser power 0.6 W shows that the damage to the surrounding tissue and skin surface decreased with increasing r_{rat} in Case 2, which was opposite to the observations made in Case 1 (see Fig. 3b). It is worth noting that Case 2 required shorter time to achieve complete tumour ablation than in Case 1.

Further comparisons between Cases 1 and 2 can be made when comparing the rate of thermal damage formation inside the tumour, as shown by the plot of *PD* against time in Fig. 6. All values of r_{rat} in Case 2 (dashed line) showed a more rapid thermal damage formation compared to Case 1 (solid line). This is reflected in the steepness of the gradient of each curve, where a steeper rise in *PD* implies a more rapid ablation of the tumour. For better comparison, a new parameter t_a was introduced:

$$t_a = t_f - t_i, \tag{14}$$

where t_f is the time at which the tumour reaches a *PD* value of 100%, i.e., complete thermal damage of the tumour, and t_i is the time at which thermal damage inside the tumour first occurs. One may view t_a as the duration required for the tumour to sustain complete thermal damage. Hence, a shorter t_i implies a more intense and rapid heating, while a longer t_a suggests that heating is either less intense or not as uniform.

The values of t_i, t_f and t_a for all cases at a laser power of 0.6 W are presented in Table 4 for ease of comparison. In Case 1, t_a decreased with increasing r_{rat}. This is to be expected, as more heat is

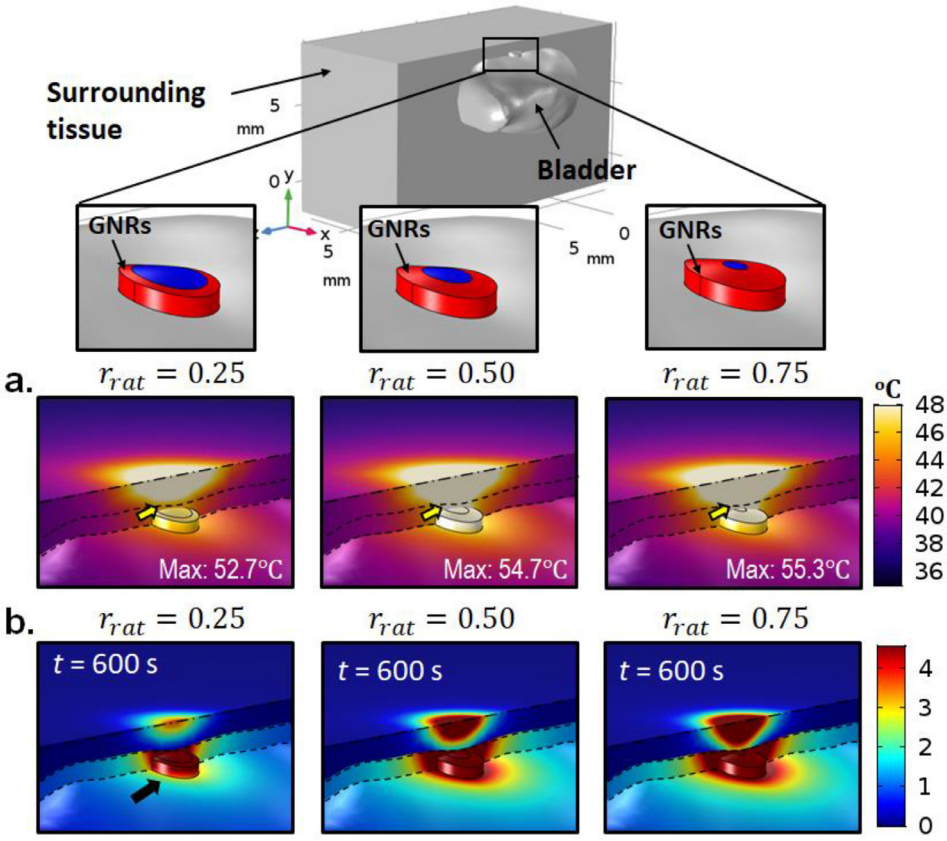

Fig. 4. a) Contours of temperature distribution at $t = 30$ s and b) contours of the thermal damage parameter Ω at $t = 600$ s for all values of r_{rat} in Case 2 across the tumour, bladder and across the surrounding tissue after laser irradiation of 0.5 W. The temperature scale of a) was capped at 48 °C for better visualisation. The colour scale of b) shows the values of Ω capped at 4.6 such that regions in dark red represent regions that are thermally damaged. The black arrow refers to incomplete tumour ablation. Top and bottom dashed lines indicate the outer and inner walls of the bladder, respectively. Dashed-dotted lines indicate the surface of the surrounding tissue.

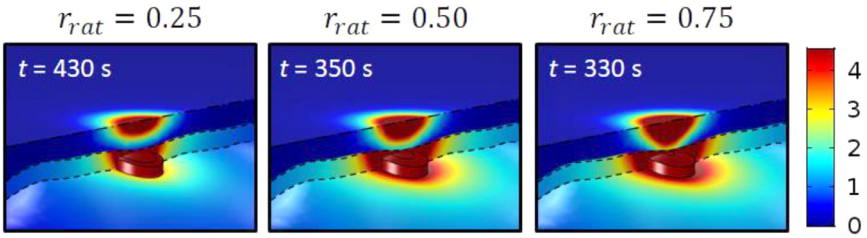

Fig. 5. Contours of the thermal damage parameter Ω for all values of r_{rat} for Case 2 across the tumour, bladder, and across the surrounding tissue at $P_{laser} = 0.6$ W when complete tumour ablation was achieved. Colour scale shows the values of Ω capped at 4.6 such that regions in dark red represent regions that are thermally damaged. Top and bottom dashed lines indicate the outer and inner walls of the bladder, respectively. Dashed-dotted lines indicate the top surface of the surrounding tissue, i.e., the skin surface.

Table 4
Summary of t_i, t_f, and t_a values for all cases at a laser power of 0.6 W.

Parameter	t_i (s)	t_f (s)	t_a (s)
Case 1			
$r_{rat} = 0.25$	440	–	–
$r_{rat} = 0.5$	300	520	220
$r_{rat} = 0.75$	230	440	210
Control	150	310	160
Case 2			
$r_{rat} = 0.25$	320	430	110
$r_{rat} = 0.5$	220	350	130
$r_{rat} = 0.75$	180	330	150
Case 3	380	460	80

generated inside the tumour due to the increase in the quantity of GNRs inside the tumour as r_{rat} increases. Consequently, this shortens the duration required for complete tumour ablation. In Case 2, t_a increased with increasing r_{rat}. As r_{rat} increases, more heat is generated around the tumour periphery. However, this also causes greater heat conduction to the bladder and the surrounding tissue due to the larger thermal gradient between the tumour and those tissues. Heat conduction towards the tumour centre may not be as efficient due to heating also from the skin surface, which created a smaller thermal gradient from the tumour periphery to the tumour centre.

An additional point can be made from Fig. 6. Despite having a smaller surface area, $r_{rat} = 0.25$ for Case 2 (0.359 mm^2) achieved a complete tumour ablation marginally quicker than for Case 1 for $r_{rat} = 0.75$ (0.455 mm^2), see black arrow. Furthermore, both the damage to the bladder and the surrounding tissue surface are lower for Case 2, $r_{rat} = 0.25$. By positioning the GNRs at the far edges of the tumour, heat is generated along those edges. When paired with the heat from the skin surface, the tumour is heated gradually but uniformly across its entirety. The gradual heating

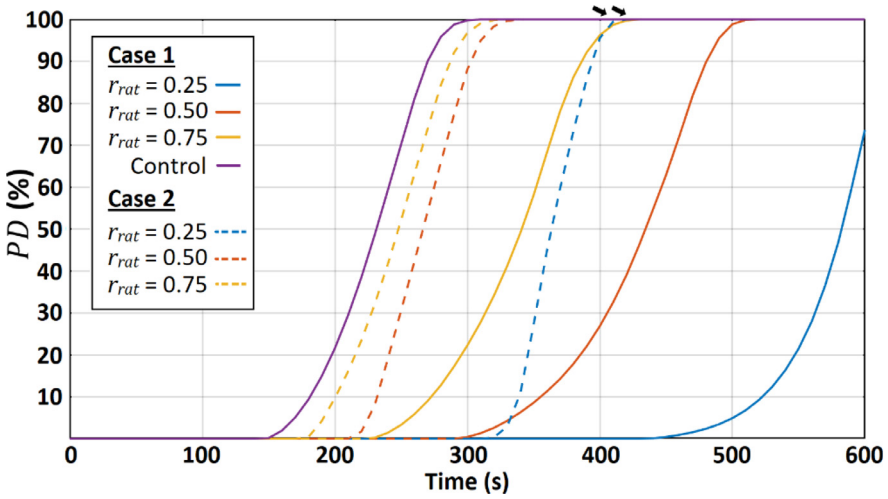

Fig. 6. Quantification of tumour damage for all values of r_{rat} for 600 s of laser irradiation at 0.6 W for Cases 1 (solid line) and 2 (dashed line).

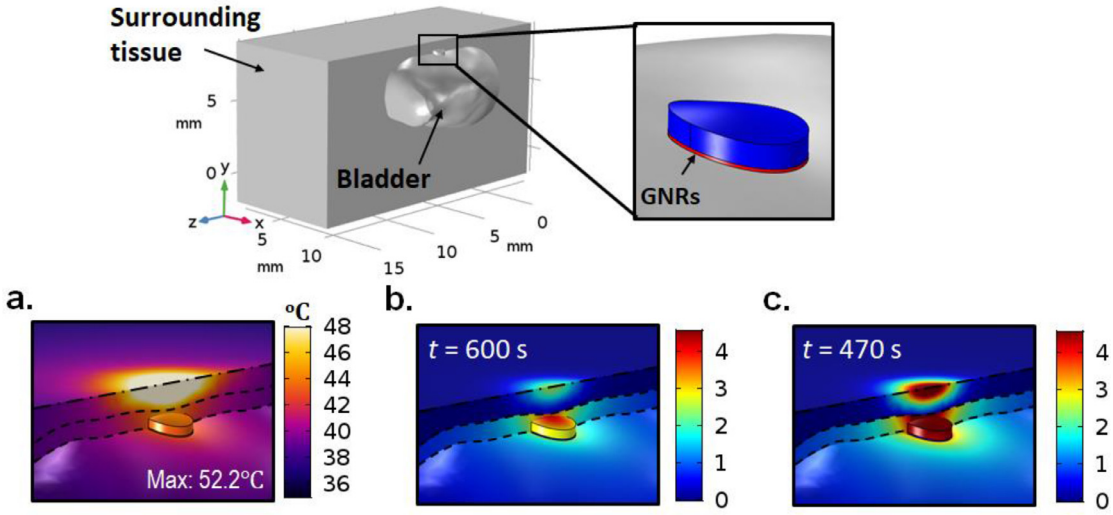

Fig. 7. a) Thermal distribution in °C for Case 3 after 30 s of laser irradiation at a laser power of 0.5 W with the temperature scale capped to 48 °C for better visualisation; b) contours of thermal damage parameter Ω for Case 3 after 600 s laser irradiation at a laser power of 0.5 W; c) contours of thermal damage parameter Ω for Case 3 at the respective time required for complete ablation at a laser power of 0.6 W. The colour scale in b) and c) shows the values of Ω capped at 4.6 such that regions in dark red represent regions that are thermally damaged. Top and bottom dashed lines indicate the outer and inner walls of the bladder, respectively. Dashed-dotted lines indicate the top surface of the surrounding tissue, i.e., the skin surface.

reduces the risk of damage to the surrounding tissues while the uniformity decreases the value of t_a. Therefore, this creates the optimal environment for the tumour to be ablated with minimal damage to the bladder and the surrounding tissue.

3.3. Case 3

Case 3 investigates the distribution of GNRs when they are attached to the surface of the tumour following intravesical instillation. Figs. 7a and 7b show the temperature distribution and thermal damage obtained for Case 3 at a laser power of 0.5 W. As expected, the assumption that GNRs are at the tumour surface resulted in heating at that region. Consequently, thermal damage begins to form along the surface and spreads towards the central and inner parts of the tumour. Although the surface area exposed to the incident laser is larger than that of Cases 1 and 2, complete tumour ablation was not achieved. While it is difficult to ascertain the exact reason, there are three potential contributing factors to this outcome.

The first factor is the distance between the incident laser and the GNRs. As the GNRs were located towards the bottom of the tumour, the distance between the GNRs and the laser increases. This means that photons from the laser are required to travel a greater distance and undergo more scattering before they reach the GNRs. This decreases the amount of light (energy) that reaches the GNRs. The second factor is the total amount of GNRs used. Since GNRs occupy only a thin layer, there were fewer GNRs present for the absorption of light. The third factor is the effect of natural convection inside the bladder. The GNRs in Cases 1 and 2 were located throughout the entire depth of the tumour, therefore, the laser light is absorbed inside the tumour and converted to heat. The effect of cooling by natural convection in urine was not as significant in Cases 1 and 2, as in Case 3 where the GNRs were directly in contact with the urine inside the bladder.

Simulations were repeated using a laser power of 0.6 W and the subsequent thermal damage obtained is presented in Fig. 7c. At this laser power, Case 3 achieved complete tumour ablation within 470 s of laser irradiation and recorded the least amount of damage to the bladder, at approximately 4.5 to 6 times smaller in terms

of volume than in Cases 1 and 2, and the control. In addition, the damage at the surrounding tissue surface was recorded to be the second lowest, marginally behind Case 2, $r_{rat} = 0.25$. In Cases 1 and 2, the damage in the bladder occurs directly above the centre of the tumour. This is because heating was the greatest between the top of the tumour and the surrounding tissue surface. However, because heating in Case 3 is located at the bottom of the tumour, a longer time is needed before the bladder can reach the high temperatures required for it to be ablated. These results demonstrate that the attachment of GNRs along the surface in-line with the inner bladder wall can decrease the amount of unwanted thermal ablation of the bladder and surrounding tissue.

4. Discussion

The present study has demonstrated that the distribution of GNRs can significantly alter the treatment effects of GNR-PTT of bladder cancer. Case 1 refers to a model in which the GNRs were homogeneously distributed at the tumour centre, with the different value of r_{rat} representing different levels of GNR spreading following intratumoural or IV injection. In Case 2, a hypothetical distribution in which the GNRs were assumed to occupy the outer regions of the tumour was investigated. Finally, Case 3 investigated the distribution of GNRs at the tumour surface along the inner wall of the bladder, representing the administration of GNRs through intravesical instillation. The results demonstrated that the location and occupancy of GNRs significantly affect the heating profile and formation of thermal damage inside the tumour. The results from Case 1 study demonstrated that the heating mechanism of GNR-PTT is a combination of heating occurring at two distinct locations: 1) at the skin surface where the laser is applied, and 2) at the region of tumour containing GNRs. These findings were reinforced and reiterated when comparing the temperature distributions obtained between Cases 2 and 3.

In the current models, the centre of laser irradiation was set to be directly in line with the central axis of the tumour, leading to a fixed power density in the bulk of the tumour in the three cases. There are two main volumes where heat generation takes place, the heating due to GNRs located at the tumour centre (Case 1) and heating in the tissue close to skin where the laser light is applied. The heat generated raises the temperature in the region between these two volumes. This is undesirable as there is a higher likelihood of unwanted ablation. In comparison, when GNRs are in the outer regions of the tumour (Case 2), heating from the laser beam complements the heating at the GNRs by supplying heat to the inner region of the tumour. This provides almost uniform heating across the entire tumour. For Case 3, the GNRs are the farthest away from the incident laser. However, because the tumour is located between the two main heating volumes, the tumour is heated from two sides. Like for Case 2, this results in a very uniform heating throughout the tumour.

The outcome of intratumoural or IV injection at the tumour centre (Case 1) significantly depends on the diffusion/permeation of GNRs inside the tumour. If the GNRs are concentrated only at the tumour centre, a laser power of 0.6 W is sufficient to achieve complete tumour ablation. However, an increase in the laser power increases the risk of damage to the bladder and surrounding tissue. In addition, this would result in highly irregular heating within the tumour and can cause significant levels of over-ablation. As such, it is desirable to avoid the case where the GNRs are not well spread throughout the tumour. Although GNRs have been found to be able to permeate through skin and various tissues, the ease of permeation is dependant on the type of tissue and the size of GNRs [51]. Larger GNRs or a highly complex tumour vasculature may impede the ability of the GNRs to spread to the outer regions of the tumour [51]. While it is convenient to suggest the use of smaller GNRs to overcome this issue, altering the dimensions of GNRs will result in different levels of heating at different laser wavelengths. Alternatively, one can consider cell-mediated delivery systems, such as macrophages to improve the GNR uptake into the tumour [52].

Among all the cases investigated, only Case 2 with $r_{rat} = 0.5$ and 0.75 were successful in attaining complete tumour ablation at a laser power of 0.5 W. Despite being 20 s slower to reach complete tumour ablation, $r_{rat} = 0.5$ recorded less damage to the bladder and no damage to the skin surface tissue when compared to $r_{rat} = 0.75$. This suggests that it is possible to minimise over-ablation while maintaining complete tumour ablation if the GNRs can be accurately distributed along the outer regions of the tumour. At a laser power of 0.6 W, all cases were able to completely ablate the tumour except for Case 1, $r_{rat} = 0.25$ due to insufficient amount of GNRs. It is worth noting that all cases with complete tumour ablation at a laser power of 0.5 W achieved less damage to the surrounding tissue surface, but larger damage to the bladder when compared to the case when 0.6 W is used. Specifically, this refers to Case 2, $r_{rat} = 0.5$ and 0.75 and the control case. Because a lower laser power was used, the ablation duration was significantly increased (by over 160 s). This caused the bladder to be exposed to heating much longer than the cases when a higher laser power was employed. Hence, using a higher laser power can decrease the damage to the bladder at the cost of greater damage to the skin surface.

The results demonstrated that increasing r_{rat} in Case 1 resulted in quicker ablation with larger damage to the bladder and less damage to the surrounding tissue and the skin surface. On the other hand, increasing r_{rat} in Case 2 results in quicker ablation with larger damage to both the bladder and at the surrounding tissue surface. Without prioritising the speed of ablation, the optimal selection between Cases 1 and 2 for this study would be Case 2, $r_{rat} = 0.25$ at a laser power of 0.6 W. This provides the least thermal damage to the bladder, the surrounding tissue and the skin surface. Furthermore, Case 2 is generally more favourable than Case 1 as the uniform heating profile results in reduced over-ablation. The scenario assumed in Case 2 relies on the ability to distribute GNRs around the tumour periphery. While this has not been specifically studied, there are various ways that this can be implemented. For example, intratumoural injection can be performed around the outer edges of the tumour instead of at the centre. Alternatively, it might be possible to employ the use of GNRs that are bio-conjugated with cancer-targeting antibodies [11–13]. Since GNRs can permeate through tissues, it might be possible to inject bio-conjugated GNRs around the tumour periphery and allowing for it to diffuse/permeate into the tumour centre. The ability to encapsulate the tumour in GNRs will allow for greater variance in treatment procedures and outcomes for both GNR-PTT and other nanoparticle applications.

The results of Case 3 clearly demonstrate that the localisation of GNRs across the surface of the tumour can successfully achieve complete tumour ablation. In addition, the thermal damage to the bladder was found to be significantly lower than in the other cases. When comparing the results of Case 3 with the other two cases, it was found that at 0.6 W, Case 3 took the longest time ($t_i = 380$ s) for the first signs of thermal damage to occur (see Table 4). Despite that, Case 3 has the shortest t_a value of only 80 s. This duration is close to Case 2, $r_{rat} = 0.25$, which recorded $t_a = 110$ s. Interestingly, both configurations obtained the least amount of over-ablation in both the bladder and the surrounding tissue surface. In contrast, the control, which recorded the quickest occurrence of damage at $t_i = 150$ s with $t_a = 160$ s, resulted in the greatest amount of damage to the bladder.

From this, a key inference can be drawn, whereby the ideal scenario to achieve complete tumour ablation with minimal damage

to the surrounding tissue is through quick but uniform ablation. The control had the most intense heating, which led to quicker formation of thermal ablation. However, because the heating was not uniform, a longer time of t_a =160 s was required before ablation was complete. This means that the surrounding tissue was subjected to higher temperatures for a total of 160 s. In Case 3 (or Case 2, r_{rat} = 0.25), the heating process was gradual. This meant that the formation of thermal damage was slower, but the overall tumour temperature raised uniformly. Hence, both the tumour and surrounding tissue were subjected to high temperatures for a shorter time (80 s for Case 3 and 110 s for Case 2, r_{rat} = 0.25). While it is difficult to control the heat generation within the tumour, future studies should focus on this aspect as the outcome may lead to the complete preservation of the surrounding tissues during GNR-PTT. One method that could be investigated in the future is by using several lasers that are positioned at different points with their beams focusing on the tumour.

All three cases investigated in the present study have demonstrated their potential for use in GNR-PTT. Case 1 has an effective and direct treatment procedure that can destroy the tumour if the spreading of GNRs can be ensured. However, intratumoural injection risks tumour track seeding or displacement as the injection needle will be directly in contact with tumour. Case 2 represents a hypothetical scenario that may require a more complex procedure to administer GNRs such that it spreads from the tumour periphery to the centre. This will also be subject to the accessibility of the tumour and the ability to accurately inject the GNRs surrounding the tumour. Case 3 has demonstrated good ability to destroy the tumour while minimising over-ablation. Although the administration of GNRs would not require direct contact with the tumour, it may not necessarily be the best approach. Yang et al. [19] found that there were GNRs that did not attach to the tumour and instead, were found in different parts of the bladder. This led to unwanted ablation as the GNRs would receive light and ablate those healthy tissues. As such, further investigations are required to overcome the above challenges.

The current study was able to investigate the thermal responses and effects of heterogeneous distributions of GNRs. Several limitations in this study must be addressed in the future. Firstly, Case 3 was modelled as a thin layer of GNR as opposed to being a surface application at the tumour. Due to computational limitations, it was not possible to assign the presence of GNRs across the tumour surface with near-zero thickness. To account for this, this region was assumed to be as thin as computationally possible without incurring any meshing issues. While steps were taken to reduce the size of the thin layer, it is possible that the current values obtained may be an overestimation of the actual scenario, though the thickness of the layer may be of similar magnitude due to diffusion. Nonetheless, the concept presented in Case 3 should remain valid as the source of heating would still come from the tumour surface. Any decrease in heating can potentially be dealt with by increasing the laser power. Secondly, results in the present study are dependant on heat generation at the skin surface. This is due to the geometry of the mice bladder that has a very thin skin thickness. Any increase in skin thickness would result in greater scattering of photons and lower absorption by the GNRs [24]. This can result in greater heating at the surrounding tissue surface and weaker heating inside the tumour. Similarly, the present study assumes the tumour to be located at the part of the bladder closest to the skin surface where laser beam is introduced. It is possible for the tumour to be located elsewhere along the bladder lining, a situation that would reduce the influence of the heating component from the surrounding tissue surface and the treatment outcome would become primarily dependant on the heating inside the tumour [24]. Thirdly, the present study assumed the use of bioconjugated GNRs such that they bind specifically to tumour cells and do not have the capacity to either aggregate or dispersed within the tissue. The ability of these GNRs to aggregate and disperse within the tissue should be explored through further laboratory studies. If such an event does occur, then a correction factor could be applied to the optical energy absorption during the simulation procedure. Finally, the current study employs a superficial tumour in the shape of a cylinder. However, actual tumours can be irregularly-shaped and may not allow for the desired distributions of GNRs to be achieved.

5. Conclusions

The present study investigated the effects of heterogeneous distribution of GNRs in different locations of the tumour for GNR-PTT. Case 1 demonstrated that the spreading of GNRs through intratumoural injection at the centre of the tumour can significantly alter the treatment outcome. Insufficient spreading can render the treatment ineffective and can be dealt with by increasing the laser power, which increases the risk of potentially inducing significant over-ablation of healthy tissues. Case 2 investigated the effects of GNRs located in the outer regions of the tumour. It was found that this configuration significantly changed the heating profile of the tumour which resulted in a more uniform heating. Consequently, damage to the bladder and the surrounding tissue could be reduced. Lastly, Case 3 investigated the presence of GNRs located at the tumour surface, which would be administered via intravesical instillation.

Results from the present study demonstrated that the administration of GNRs via bladder instillation can achieve complete tumour ablation. In addition, this method may be better than intratumoural injection as it requires no direct contact with the tumour. Findings from the present study demonstrated that the presence of a thin layer of GNRs across the luminal side of the tumour following intravesical instillation presents no concern of incomplete tumour ablation. In fact, intravesical instillation possesses some advantages over intratumoural injection or IV method and may serve as the impetus for further development of this technique, especially for bladder cancer treatment in human.

Declaration of competing interest

None declared.

Acknowledgement

This study has received funding from the European Union's Horizon 2020 research and innovation program under grant agreement No 801126 (EDIT).

APPENDIX A

The absorption and scattering coefficients of tumour with GNR were calculated using the Mie-Gans theory [47], which solves the Maxwell equations based on an electrostatic assumption. This assumption is valid for $D \leq \lambda/10$, where D is the diameter of the GNR and λ is the wavelength of the laser irradiation. Accordingly, the absorption and scattering coefficients of a medium embedded with GNR can be calculated using [53, 54]:

$$\mu_a = \frac{2\pi\phi}{\lambda V_{np}} \text{imag}\left(\frac{\alpha_1}{3} + \frac{\alpha_2}{3} + \frac{\alpha_3}{3}\right), \tag{A.1}$$

$$\mu_s = \frac{16\pi^3\phi}{18\lambda^4 V_{np}} \left(|\alpha_1|^2 + |\alpha_2|^2 + |\alpha_3|^2\right), \tag{A.2}$$

where imag() represents the imaginary component, ϕ is the volume fraction of GNR, V_{np} is the volume of a single nanoparticle calculated by assuming the GNR to be a cylinder capped by hemispheres at both ends and α_i (for i =1, 2, 3) is the polarization given by [53, 54]:

$$\alpha_i = V_{np}\left[\frac{\varepsilon(\omega, D) - \varepsilon_m}{P_i(\varepsilon(\omega, D) - \varepsilon_m) + \varepsilon_m}\right], \tag{A.3}$$

where ε is the size- and frequency-dependant dielectric function of the GNR, ε_m is the dielectric constant of the surrounding medium and P_i is the geometrical factor. In the present study, the Kreibig-Vollmer model for calculating the size- and frequency-dependant dielectric function of GNR was adopted, which is given by [48, 49]:

$$\varepsilon(\omega, D) = \varepsilon_{bulk} + \omega_p^2\left(\frac{1}{\omega^2 + \Gamma_o^2} - \frac{1}{\omega^2 + \Gamma_d^2}\right) + i\frac{\omega_p^2}{\omega}\left(\frac{\Gamma_d}{\omega^2 + \Gamma_o^2} - \frac{\Gamma_o}{\omega^2 + \Gamma_d^2}\right), \tag{A.4}$$

where ε_{bulk} is the frequency-dependant dielectric constant of bulk gold, and ω_p and Γ_d are given by:

$$\omega_p = \left(\frac{n_o e^2}{\varepsilon_o m_e}\right)^{\frac{1}{2}}, \tag{A.5}$$

$$\Gamma_d = \Gamma_o + \frac{A_s v_F}{r_{eff}}, \tag{A.6}$$

$$r_{eff} = \frac{4V_{np}}{S_{np}} \tag{A.7}$$

where n_o is the electron density number, ε_o is permittivity of vacuum, e and m_e are the charge and mass of the electrons, respectively, v_F is Fermi velocity, A_s is the surface scattering parameter with an empirical value of 0.3, r_{eff} is effective radius, S_{np} is the surface area of a single nanoparticle and Γ_o is the free damping coefficient defined as the ratio of Fermi velocity and the mean free path of electrons [55]. The dielectric constant of bulk gold was obtained from data published by Johnson and Christy [48].

It should be noted that the Mie-Gans theory for calculating μ_a and μ_s is only valid for spheroidal nanoparticles where the geometrical factor used in Eq (A.3) can be obtained using:

$$P_1 = \frac{1 - e^2}{e^2}\left[\frac{1}{2e}\ln\left(\frac{1 + e}{1 - e}\right) - 1\right], \tag{A.8}$$

$$P_2 = P_3 = \frac{1}{2}(1 - P_1), \tag{A.9}$$

where $e = [1 - (D/L)^2]^{0.5}$, P_1 is orientated in the longitudinal axis of the spheroid, while P_2 and P_3 are in the transverse directions, with $P_2 = P_3$ due to symmetry. However, the nanoparticles used in this study are GNRs shaped as spherically capped cylinders. Hence, difference in geometry must be accounted for by adjusting the geometric factor used in Eq (A.3). To that extent, Prescott and Mulvaney [56] derived alternate values for P_i for GNRs which is given by:

$$\frac{1 - P_1}{P_1} = a(AR)^2 + b(AR) + c, \tag{A.10}$$

where AR is the aspect ratio of the nanoparticle and a, b and c are the coefficients of the quadratic function. For the GNR morphology used in this study, the coefficients of the quadratic function are a = 0.3504, b = 2.0809 and c = −0.3035 [56]. It is important to point out here that Eq (A.10) is purely empirical, and no physical meaning should be inferred from it.

APPENDIX B

Results from the preliminary study (see Section 3) to identify the best combination of laser power and GNR volume fraction are briefly presented here. Fig. B.1 illustrates the contours of thermal damage obtained for r_{rat} = 1 for all the combinations of P_{laser} and ϕ investigated. At ϕ = 0.001%, incomplete tumour ablation was observed for both P_{laser} = 0.4 and 0.5 W. This was confirmed from the estimation of *PD*, with values of 0 and 86.4% obtained for P_{laser} = 0.4 and 0.5 W, respectively. When ϕ was increased to 0.005%, only the case of P_{laser} = 0.5 W resulted in complete tumour ablation, with *PD* values calculated to be 10 and 100% for P_{laser} = 0.4 and 0.5 W, respectively. Since r_{rat} = 1 represents the largest possible heating that can be achieved during GNR-PTT when compared to smaller values of r_{rat}, it was decided to select the combination of laser power of at least 0.5 W and a GNR volume fraction of 0.01% for the analysis of the present study.

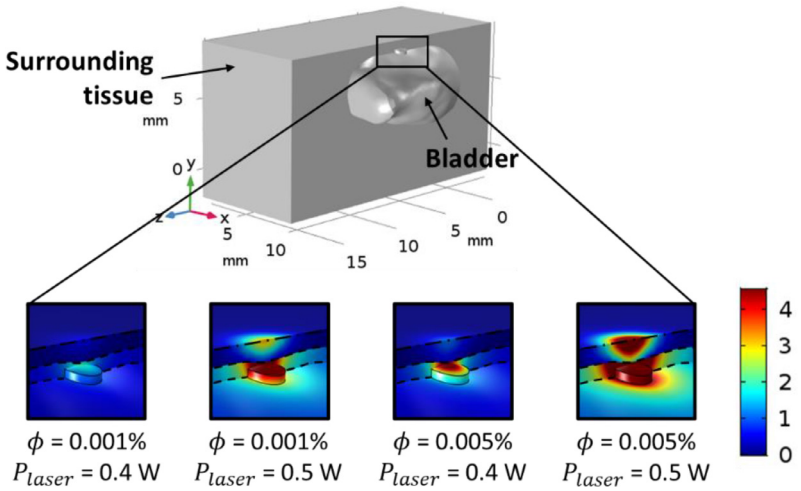

Fig. B.1. Contours of the thermal damage parameter Ω obtained after 600 s of laser irradiation for different values of P_{laser} and ϕ for the case where r_{rat} = 1. Complete tumour ablation was observed only for the case where P_{laser} = 0.5 W and ϕ = 0.005%. Top and bottom dashed lines indicate the outer and inner walls of the bladder, respectively. Dashed-dotted lines indicate the surface of the surrounding tissue.

References

[1] R. Zhou, M. Zhang, J. Xi, J. Li, R. Ma, L. Ren, Z. Bai, K. Qi, X. Li, Gold nanorods-based photothermal therapy: interactions between biostructure, nanomaterial, and near-infrared irradiation, Nanoscale Res. Lett. 17 (2022) 68.

[2] Z. Yang, Z. Sun, Y. Ren, X. Chen, W. Zhang, X. Zhu, Z. Mao, J. Shen, S. Nie, Advances in nanomaterials for use in photothermal and photodynamic therapeutics (Review), Mol. Med. Rep. 20 (2019) 5–15.

[3] F. Zhou, D. Xing, Z. Ou, B. Wu, D.E. Resasco, W.R. Chen, Cancer photothermal therapy in the near-infrared region by using single-walled carbon nanotubes, J. Biomed. Opt. 14 (2009) 021009.

[4] A.J. Trinidad, S.J. Hong, Q. Peng, S.J. Madsen, H. Hirschberg, Combined concurrent photodynamic and gold nanoshell loaded macrophage-mediated photothermal therapies: an in vitro study on squamous cell head and neck carcinoma, Lasers Surg. Med. 46 (2014) 310–318.

[5] P. Liu, W. Yang, L. Shi, H. Zhang, Y. Xu, P. Wang, G. Zhang, W.R. Chen, B. Zhang, X. Wang, Concurrent photothermal therapy and photodynamic therapy for cutaneous squamous cell carcinoma by gold nanoclusters under a single NIR laser irradiation, J. Mater. Chem. B 7 (2019) 6924–6933.

[6] H.S. Kim, D.Y. Lee, Near-infrared-responsive cancer photothermal and photodynamic therapy using gold nanoparticles, Polymers (Basel) 10 (2018) 961.

[7] Y. Wang, K.C.L. Black, H. Luehmann, W. Li, Y. Zhang, X. Cai, D. Wan, S.-Y. Liu, M. Li, P. Kim, Z.-Y. Li, L.V. Wang, Y. Liu, Y. Xia, Comparison study of gold nanohexapods, nanorods, and nanocages for photothermal cancer treatment, ACS Nano 7 (2013) 2068–2077.

[8] X. Gu, V. Timchenko, G. Yeoh, L. Dombrovsky, R. Taylor, The effect of gold nanorods clustering on near-infrared radiation absorption, Appl. Sci. 8 (2018) 1132.

[9] M.A. Mackey, M.R.K. Ali, L.A. Austin, R.D. Near, M.A. El-Sayed, The most effective gold nanorod size for plasmonic photothermal therapy: theory and in vitro experiments, J. Phys. Chem. B 118 (2014) 1319–1326.

[10] A.C.V. Doughty, A.R. Hoover, E. Layton, C.K. Murray, E.W. Howard, W.R. Chen, Nanomaterial applications in photothermal therapy for cancer, Materials (Basel) 12 (2019) 779.

[11] R.T. Busch, F. Karim, J. Weis, Y. Sun, C. Zhao, E.S. Vasquez, Optimisation and structural stability of gold nanoparticle-antibody bioconjugates, ACS Omega 4 (2019) 15269–15279.

[12] S.K. Cho, K. Emoto, L.J. Su, X. Yang, T.W. Flaig, W. Park, Functionalised gold nanorods for thermal ablation treatment of bladder cancer, J. Biomed. Nanotechnol. 10 (2014) 1267–1276.

[13] C.H. Chen, Y.-J. Wu, J.-J. Chen, Gold Nanotheranostics: photothermal Therapy and imaging of mucin 7 conjugated antibody nanoparticles for urothelial cancer, Biomed. Res. Int. 2015 (2015) 813632.

[14] R.V. Nair, H. Santhakumar, R.S. Jayasree, Gold nanorods decorated with a cancer drug for multimodal imaging and therapy, Farad. Discuss. 207 (2018) 423–435.

[15] N. Narayanan, J.H. Kim, H. Santhakumar, M.M. Joseph, V. Karunakaran, S. Shamjith, G. Saranya, P.T. Sujai, R.S. Jayasree, I. Barman, K.K. Maiti, Nanoteranostic probe built on methylene blue loaded cucurbituril [8]and gold nanorod: targeted phototherapy in combination with sers imaging on breast cancer cells, J. Phys. Chem. B 125 (2021) 13415–13424.

[16] R.V. Nair, D.L.V. Nair, D.M. Govindachar, H. Santhakumar, S.S. Nazeer, C.R. Rekha, S.J. Shenoy, G. Periyasamy, R.S. Jayasree, Luminescent gold nanorods to enhance the near-infrared emission of a photosensitizer for targeted cancer imaging and dual therapy: experimental and theoretical approach, Chem. A Eur. J. 26 (2020) 2826–2836.

[17] R.V. Nair, M.F. Puthiyaparambath, R. Chatanathodi, L.V. Nair, R.S. Jayasree, A nanoarchitecture of a gold cluster conjugated gold nanorod hybrid system and its application in fluorescence imaging and plasmonic photothermal therapy, Nanoscale 17 (2022) 13561–13569.

[18] E. Alchera, M. Monieri, M. Maturi, I. Locatelli, E. Locatelli, S. Tortorella, A. Sacchi, A. Corti, M. Nebuloni, R. Lucianò, F. Pederzoli, F. Montorsi, A. Salonia, S. Meyer, J. Jose, P. Giustetto, M.C. Franchini, F. Curnis, M. Alfano, Early diagnosis of bladder cancer by photoacoustic imaging of tumor-targeted gold nanorods, Photoacoustics 28 (2022) 100400.

[19] X. Yang, L.J. Su, F.G. La Rosa, E.E. Smith, I.R. Schlaepfer, S.K. Cho, B. Kavanagh, W. Park, T.W. Flaig, The antineoplastic activity of photothermal ablative therapy with targeted gold nanorods in an orthotopic urinary bladder cancer model, Bladder Cancer 3 (2017) 201–210.

[20] R. Ge, Z. Wang, L. Cheng, Tumor microenvironment heterogeneity an important mediator of prostate cancer progression and therapeutic resistance, Npj Precis. Oncol. 6 (2022) 31.

[21] E.H. Ooi, V. Popov, M. Alfano, J.K.K. Cheong, Influence of natural convection on gold nanorods-assisted photothermal treatment of bladder cancer in mice, Int. J. Hyperthermia 37 (2020) 634–650.

[22] S. Soni, H. Tyagi, R.A. Taylor, A. Kumar, Investigation on nanoparticle distribution for thermal ablation of a tumour subjected to nanoparticle assisted thermal therapy, J. Therm. Biol. 43 (2014) 70–80.

[23] S. Soni, H. Tyagi, R.A. Taylor, A. Kumar, Role of optical coefficients and healthy tissue-sparing characteristics in gold nanorod-assisted thermal therapy, Int. J. Hyperthermia 29 (2013) 87–97.

[24] J.K.K. Cheong, V. Popov, E. Alchera, I. Locatelli, M. Alfano, L. Menichetti, P. Armanetti, M. Maturi, M.C. Franchini, E.H. Ooi, Y.S. Chiew, A numerical study to investigate the effects of tumour position on the treatment of bladder cancer in mice using gold nanorods assisted photothermal ablation, Comput. Biol. Med. 138 (2021) 104881.

[25] V. Periyasamy, M. Pramanik, Advances in Monte Carlo simulation for light propagation in tissue, IEEE Rev. Biomed. Eng. 10 (2017) 122–135.

[26] S. Song, Y. Kobayashi, M. Fujie, Monte-Carlo simulation of light propagation considering characteristic of near-infrared led and evaluation on tissue phantom, Procedia CIRP 5 (2013) 25–30.

[27] A.A. Leino, A. Pulkkinen, T. Tarvainen, ValoMC: a Monte Carlo software and MATLAB toolbox for simulating light transport in biological tissue, OSA Continuum. 2 (2019) 957–972.

[28] H.H. Pennes, Analysis of tissue and arterial blood temperatures in the resting human forearm, J. Appl. Physiol. 1 (1948) 93–122.

[29] E.H. Wissler, Pennes' 1948 paper revisited, J. Appl. Physiol. 85 (1998) 35–41.

[30] F.C. Henriques Jr, Studies of thermal injury; the predictability and the significance of thermally induced rate processes leading to irreversible epidermal injury, Am. J. Pathol. 43 (1947) 489–502.

[31] I.A. Chang, Considerations for thermal injury analysis for RF ablation devices, Open Biomed. Eng. J. 4 (2010) 3–12.

[32] M. Trujillo, J. Bon, M. José Rivera, F. Burdío, E. Berjano, Computer modelling of an impedance-controlled pulsing protocol for RF tumour ablation with a cooled electrode, Int. J. Hyperthermia 32 (2016) 931–939.

[33] P.A. Hasgall, F. Di Gennaro, C. Baumgartner, E. Neufeld, B. Lloyd, M.C. Gosselin, D. Payne, A. Klingenböck and N. Kuster, IT'IS Database for thermal and electromagnetic parameters of biological tissues, Version 4.1, Feb 22, 2022, doi:10.13099/VIP21000-04-1. itis.swiss/database.

[34] X. He, S. McGee, J.E. Coad, F. Schmidlin, P.A. Iaizzo, D.J. Swanlund, S. Kluge, E. Rudie, J.C. Bischof, Investigation of the thermal and tissue injury behaviour in microwave thermal therapy using a porcine kidney model, Int. J. Hyperthermia 20 (2004) 567–593.

[35] N.M. Dimitriou, A. Pavlopoulou, I. Tremi, V. Kouloulias, G. Tsigaridas, A.G. Georgakilas, Prediction of gold nanoparticle and microwave-induced hyperthermia effects on tumor control via a simulation approach, Nanomaterials 9 (2019) 167.

[36] X. He, S. Bhowmick, J.C. Bischof, Thermal therapy in urologic systems: a comparison of arrhenius and thermal isoeffective dose models in predicting hyperthermic injury, J. Biomech. Eng. 131 (2009) 074507.

[37] J. Pearce, Mathematical models of laser-induced tissue thermal damage, Int. J. Hyperthermia 27 (2011) 741–750.

[38] N. Wright, On a relationship between the arrhenius parameters from thermal damage studies, J. Biomech. Eng. 125 (2003) 300–304.

[39] E.H. Ooi, E.Y.K. Ng, Simulation of aqueous humor hydrodynamics in human eye heat transfer, Comput. Biol. Med. 38 (2008) 252–262.

[40] G. von Maltzahn, J.-H. Park, A. Agrawal, N.K. Bandaru, S.K. Das, M.J. Sailor, S.N. Bhatia, Computationally guided photothermal tumor therapy using long–circulating gold nanorod antennas, Cancer Res. 69 (2009) 3892–3900.

[41] M. Trujillo, E. Berjano, Review of the mathematical functions used to model the temperature dependence of electrical and thermal conductivities of biological tissue in radiofrequency ablation, Int. J. Hyperthermia 29 (2013) 590–597.

[42] C. Rossman, D. Haemmerich, Review of temperature dependence of thermal properties, dielectric properties, and perfusion of biological tissues at hyperthermic and ablation temperatures, Crit. Rev. Biomed. Eng. 42 (2014) 467–492.

[43] D.J. Schutt, D. Haemmerich, Effects of variation in perfusion rates and of perfusion models in computational models of radio frequency tumor ablation, J. Med. Phys. 35 (2008) 3462–3470.

[44] J.L. Sandell, T.C. Zhu, A review of in-vivo optical properties of human tissues and its impact on PDT, J. Biophotonics 4 (2011) 773–787.

[45] I. Rafailov, V. Dremin, K. Litvinova, A. Dunaev, S. Sokolovski, E. Rafailov, Computational model of bladder tissue based on its measured optical properties, J. Biomed. Opt. 21 (2016) 025006.

[46] L. Wang, S.L. Jacques, L. Zheng, MCML-Monte Carlo modeling of light transport in multi-layered tissues, Comput. Methods Programs Biomed. 47 (1995) 131–146.

[47] R. Gans, Über die Form ultramikroskopischer Silberteilchen, Ann. Phys. (N Y) 352 (1915) 270–284.

[48] P.B. Johnson, R.W. Christy, Optical constants of the noble metals, Phys. Rev. B 6 (1972) 4370–4379.

[49] A.N. Bashkatov, E.A. Genina, V.I. Kochubey, V.V. Tuchin, Optical properties of human skin, subcutaneous and mucous tissues in the wavelength range from 400 to 2000 nm, J. Phys. D: Appl. Phys 38 (2005) 2543–2555.

[50] M. Nikfarjam, V. Muralidharan, C. Christophi, Mechanisms of focal heat destruction of liver tumors, J. Surg. Res. 127 (2005) 208–223.

[51] G. Sonavane, K. Tomoda, A. Sano, H. Ohshima, H. Terada, K. Makino, In vitro permeation of gold nanoparticles through rat skin and rat intestine: effect of particle size, Colloid. Surf. B: Biointerfaces 65 (2008) 1–10.

[52] Z. Li, H. Huang, S. Tang, Y. Li, X.F. Yu, H. Wang, P. Li, Z. Sun, H. Zhang, C. Liu, P.K. Chu, Small gold nanorods laden macrophages for enhanced tumor coverage in photothermal therapy, Biomaterials 74 (2016) 144–154.

[53] U. Kreibig, M. Vollmer, Optical Properties of Metal Clusters, Springer-Verlag, Berlin, Germany, 1995.

[54] C. Bohren, D. Huffman, Absorption and Scattering by an Arbitrary Particle, Wiley-VCH Verlag, Germany, 2004.

[55] S.V. Gaponenko, Introduction to Nanophotonics, Cambridge University Press, Cambridge, 2010.

[56] S.W. Prescott, P. Mulvaney, Gold nanorod extinction spectra, J. Appl. Phys. 99 (2006) 123504.